Global and Planetary Change 200 (2021) 103473

Contents lists available at ScienceDirect

Global and Planetary Change

journal homepage: www.elsevier.com/locate/gloplacha

Deep-water osmium-isotope record of the Permian–Triassic interval from Niushan, China reveals potential delayed volcanic signal post the mass extinction

Zeyang Liu [a,b,c,*], David Selby [c,d]

[a] State Key Laboratory of Organic Geochemistry, Guangzhou Institute of Geochemistry, Chinese Academy of Sciences, Guangzhou 510640, China
[b] CAS Center for Excellence in Deep Earth Science, Guangzhou 510640, China
[c] Department of Earth Sciences, Durham University, Durham DH1 3LE, UK
[d] State Key Laboratory of Geological Processes and Mineral Resources, School of Earth Resources, China University of Geosciences, Wuhan 430074, Hubei, China

ARTICLE INFO

Keywords:
Osmium isotope
End Permian mass extinction
Volcanism
Weathering
South China

ABSTRACT

The end Permian mass extinction event is one of the most severe biotic crisis of the Phanerozoic. The trigger of this event has been widely linked to massive volcanic activity associated with the Siberian Traps Large Igneous Province through the application of multiple geochronological (e.g., U—Pb and Ar—Ar dating) and geochemical proxies (e.g., C, Hg, Zn, Os, etc.). Of these proxies, a few osmium ($^{187}Os/^{188}Os$) records are available for near-shore/shallow water depositional settings (e.g., Meishan, China; Opal Creek, Canada), which suggest multiple episodes of volcanism before, during and after the mass extinction event. Here, we present a new initial $^{187}Os/^{188}Os$ (Os_i) stratigraphy across the deep-water Niushan Permian–Triassic boundary interval section of South China that reveals a single unradiogenic Os-isotope shift (from ~0.6 to 0.3) after the end Permian mass extinction event interval, which is interpreted to be related to volcanic activity. Above the unradiogenic excursion, a radiogenic shift to ~1.1 is detected across the Permian–Triassic boundary at Niushan that is correlative to the radiogenic Os_i shift observed in the Meishan section. This increase in Os-isotope values is taken to reflect enhanced continental weathering. Both the unradiogenic and radiogenic excursions in the deep-water Niushan section are smaller in magnitude compared with the Os isotope profiles from more shallow-water sections of Meishan and Opal Creek. Our data suggest investigations of multiple sections across a variety of depositional environments may yield a more comprehensive understanding of the scale of the global perturbations related to volcanism and continental weathering intensity of the Permian–Triassic boundary interval.

1. Introduction

The end Permian mass extinction (EPME) event represents the most severe biotic loss of both marine and terrestrial species of the Phanerozoic (Erwin, 2006). This biotic crisis is associated with an intense disturbance in the global carbon cycle that is characterized worldwide by sedimentary sections exhibiting large negative carbon isotope excursions (see a review by Korte and Kozur, 2010). Further, during the EPME the Earth's environment witnessed global warming (Joachimski et al., 2012; Sun et al., 2012; Chen et al., 2016), oceanic acidification (Hinojosa et al., 2012; Clarkson et al., 2015; Garbelli et al., 2017; Song et al., 2021), and oceanic anoxia and/or euxinia (Wignall and Twitchett, 1996; Grice et al., 2005; Cao et al., 2009). These environmental perturbations and the mass extinction have been ultimately linked to intensive volcanism associated with the Siberian Traps Large Igneous Province (LIP) (e.g. Payne and Kump, 2007; Saunders and Reichow, 2009; Shen et al., 2013; Hu et al., 2019; Shen et al., 2019b).

Being the largest mass extinction event, the end Permian mass extinction event and the Permian–Triassic boundary (PTB) interval have been extensively studied by high-resolution biostratigraphy, high-precision dating and isotope stratigraphy (e.g. mercury and zinc isotopes; Liu et al., 2017; Wang et al., 2018, Shen et al., 2019a; Chu et al., 2020; Dal Corso et al., 2020). To date, osmium-isotope ($^{187}Os/^{188}Os$) stratigraphy for the Permian–Triassic interval are limited to the Meishan (South China) and Opal Creek (Canada) sections (Schoepfer et al., 2013; Georgiev et al., 2015; Zhao et al., 2015; Liu et al., 2020b). Osmium

* Corresponding author at: State Key Laboratory of Organic Geochemistry, Guangzhou Institute of Geochemistry, Chinese Academy of Sciences, Guangzhou 510640, China.
E-mail address: geozy.liu@outlook.com (Z. Liu).

https://doi.org/10.1016/j.gloplacha.2021.103473
Received 19 December 2020; Received in revised form 8 March 2021; Accepted 8 March 2021
Available online 13 March 2021

isotope data of the Permian–Triassic interval are also reported for the Hovea-3 section (Western Australia), however, absolute interpretation of the data suffers from potential disconformity and uncertainty in the position of the Permian–Triassic boundary (Georgiev et al., 2020).

The Meishan section hosts the Global Stratotype Section and Points (GSSPs) for the Permian–Triassic boundary and the Wuchiapingian–Changhsingian boundary (Yin et al., 2001; Jin et al., 2006). This section was deposited in a middle–upper slope setting, with an estimated water depth between 30 and 60 m (Yin et al., 2001). The Opal Creek section represents an outer-shelf or upper slope setting on the eastern of the Panthalassa Ocean at a paleolatitude of ~30°N (Henderson, 1989). A major regional unconformity is placed ~1.5 m below the Permian–Triassic boundary that separates the lower Middle Permian strata from the upper Upper Permian–Lower Triassic deposits.

Previous paleoclimate studies using Os isotopes suggest that, in response to geological events, Os isotope stratigraphy from different paleogeographic depositional settings may express discrete Os isotope composition and different magnitudes of isotope excursion (e.g. Paquay and Ravizza, 2012; Rooney et al., 2016; Liu et al., 2019b; Jones et al., 2020). In this study, we report osmium isotope stratigraphy for the Permian–Triassic boundary interval from the deep-water section Niushan section (South China), to provide further insights into the temporal relationship and magnitude of the volcanism and subsequent climate perturbation.

2. Geological background

The Niushan section outcrops in an active quarry located in Xuancheng City, Anhui Province (N31°08′57.6″, E118°49′44.9″; Figs. 1 and 2). The section comprises the Longtan, Dalong, and Yinkeng formations, and is constrained biostratigraphically by the occurrence of early Triassic ammonoids (Ophiceratidae) that occur immediately above a volcanic ash layer (Ash-6 in Fig. 2), and geochronologically by LA-ICP-MS U—Pb zircon ages (Fig. 2; Liao et al., 2016a). The correlation of the section with the Meishan section is further supported by a high-resolution organic carbon isotope stratigraphy (Liao et al., 2016a). Sample NS-107 records the lowest $\delta^{13}C_{org}$ in the Niushan section, and correlates to the extremely negative carbon isotope excursions in bed 26 of the Meishan section. Moreover, abundant calcareous and siliceous organisms (e. g., brachiopods) occur below, but not above NS-107, indicating a dramatic biotic abundance decrease across this interval (Liao et al., 2016a).

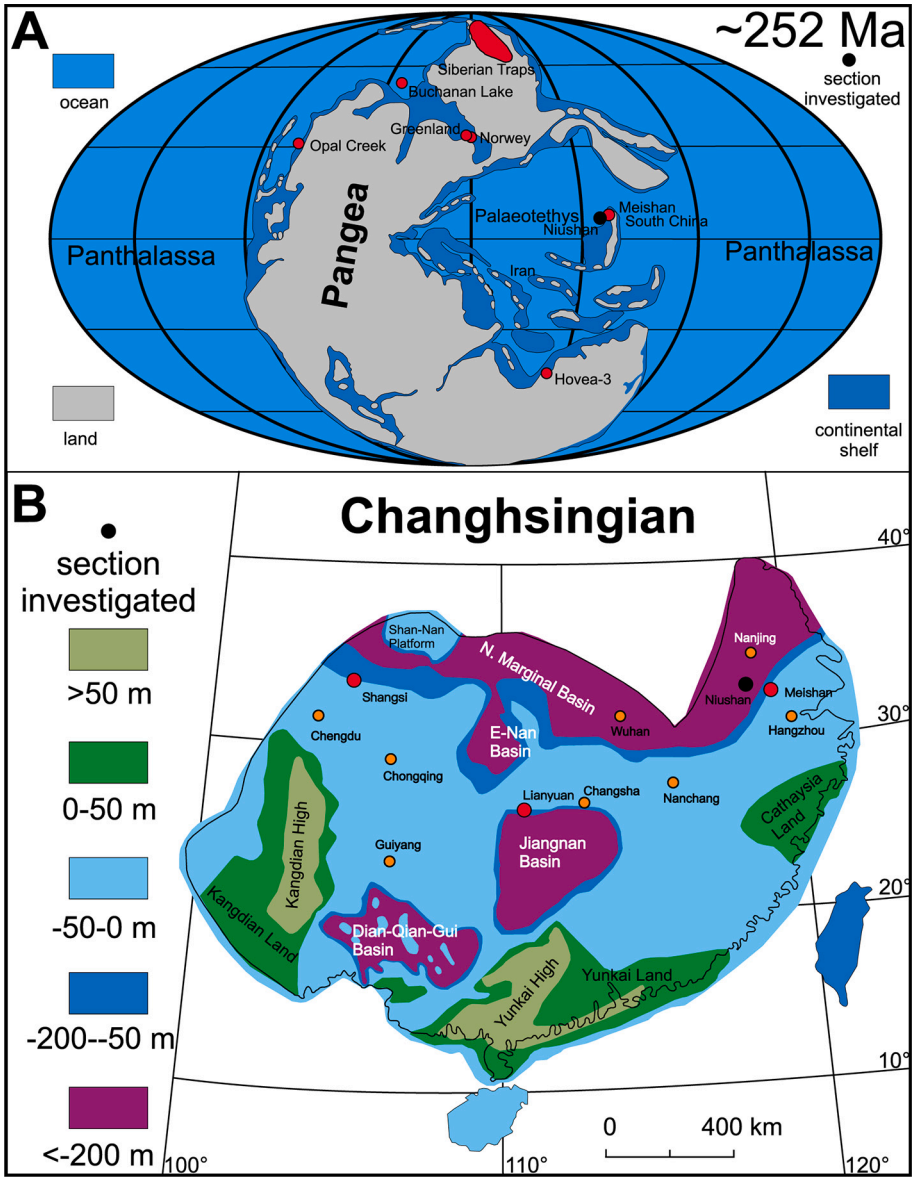

Fig. 1. Late Permian paleogeographic maps showing the studied areas. (A) Changhsingian Stage global paleogeographic reconstruction map showing the location of the Niushan, Meishan, Greenland, Norway, Buchanan Lake, Hovea-3 and Opal Creek sections; base map after Ziegler et al. (1997); (B) South China showing the paleogeographic locations of the Niushan (black circle) and Meishan, Shangsi, Lianyuan (red circle) sections; base map modified from Wang and Jin (2000). Figure modified from Liu et al. (2019b). (For interpretation of the references to colour in this figure legend, the reader is referred to the web version of this article.)

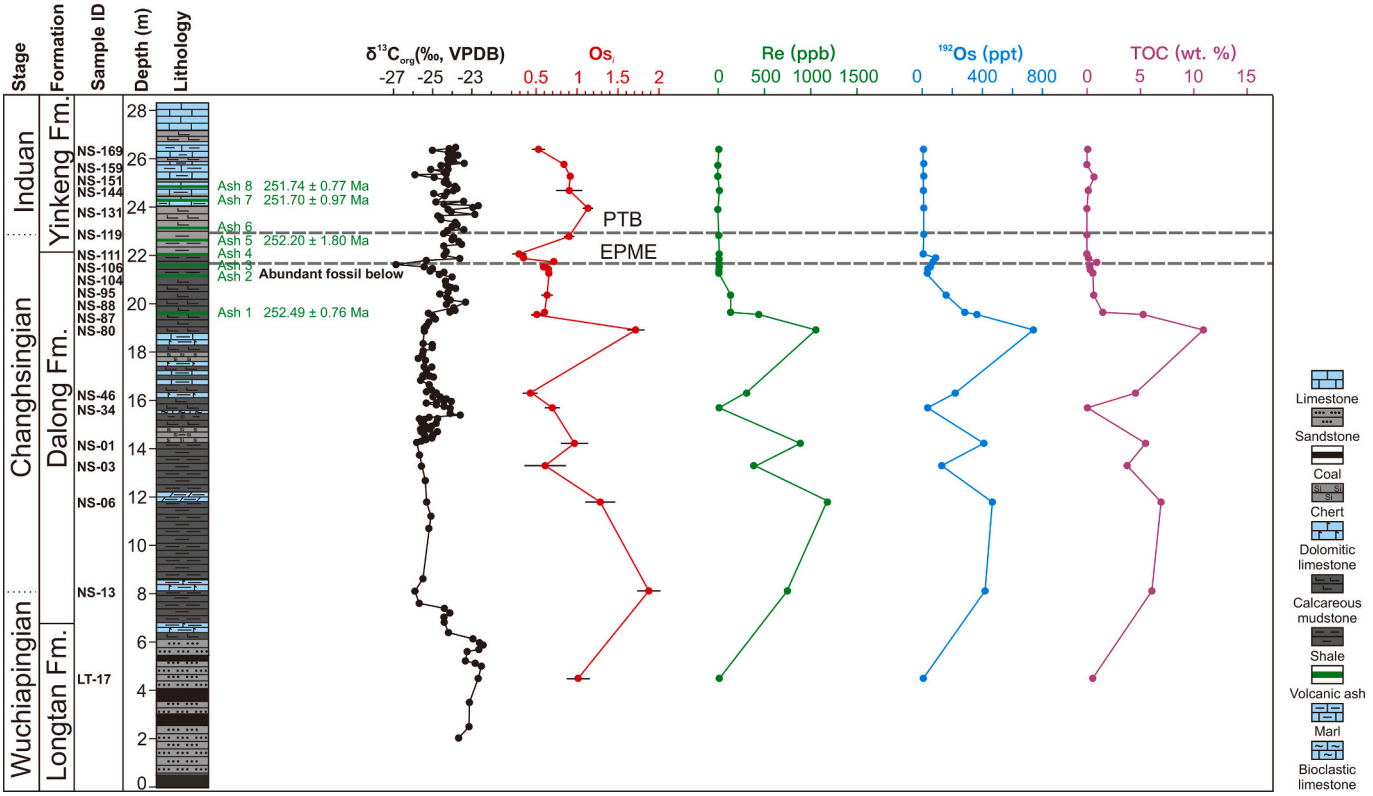

Fig. 2. Carbon isotope ($\delta^{13}C_{org}$, black), Os_i (red), Re (green) and ^{192}Os abundance (blue) stratigraphy of the Niushan section, China. The $\delta^{13}C_{org}$ data, TOC data, lithology and sea level curve are from Liao et al. (2016a). Ash layer chronology are LA-ICP-MS U—Pb Zircon ages from Liao et al. (2016a, 2016b). Ages in the column are that used to calculate each sample's Os_i, estimated with the Permian–Triassic boundary age and Wuchiapingian–Changhsingian boundary age, assuming a constant deposition rate throughout the section. EPME = end Permian Mass Extinction; PTB = Permian–Triassic Boundary. (For interpretation of the references to colour in this figure legend, the reader is referred to the web version of this article.)

The lower part of the section is recorded by the Longtan Formation which is composed of silty sandstone that is interbedded with thin coal beds in its lower part. Conformably overlying the Longtan Formation is the Dalong Formation that is dominated by organic-rich thin to medium bedded calcareous and siliceous shale, with thin interbeds of carbonate and chert. The Dalong Formation is conformably overlain by the Yinkeng Formation, which comprises mainly dark grey mudstone in its lower part and carbonate rocks in its upper part. Several volcanic ash layers occur in the upper Dalong and lower Yinkeng formations (Fig. 2). Four of these have been dated by U—Pb zircon LA-ICP-MS to be 251.74 ± 0.77 Ma, 251.70 ± 0.97 Ma, 252.20 ± 1.80 Ma and 252.49 ± 0.76 Ma (Fig. 2; Liao et al., 2016a, 2016b). The Permian–Triassic boundary is assigned to the lower part of the Yinkeng Formation. The end Permian mass extinction interval is characterized by a large negative carbon isotope excursion of ~3‰ ($\delta^{13}C_{org}$) that is correlative to $\delta^{13}C_{carb}$ and $\delta^{13}C_{org}$ profiles from other EPME sections globally. The Longtan, Dalong and Yinkeng formations of the Niushan section reflect a regional rise in sea level, with the paleoceanographic reconstruction of the WCB interval representing a fluvial/deltaic deposition and the PTB interval interpreted to record a deep-water setting with water depths >200 m (Fig. 1; Wang and Jin, 2000), which is in contrast to the Meishan section that represents a shallow/middle-upper slope depositional setting (<200 m; Wang and Jin, 2000). Present day the distance between the Niushan and Meishan sections is 90 Km. Given that no tectonism has occurred since deposition to bring the sites geographically closer, it is considered that the depositional environments/settings of the Meishan (shallow-water section) and Niushan (deep-water section) were of similar distance apart as they are present day.

3. Methods

Samples (n = 23) from the Niushan section were obtained from archived samples that were collected as part of a previous study from a freshly exposed quarry face at Niushan (Liao et al., 2016a). According to the zircon U—Pb age chronology and the carbon isotope stratigraphy of the section, sampling was aimed to encapsulate the pre, syn and post EPME interval. Samples were not collected adjacent to the stratigraphically distinct ash horizons to avoid any potential contamination of hydrogenous Re and Os with volcanic Re and Os in the sedimentary units. Each sample represents a stratigraphic interval of 1 cm. Approximately 30 g of each sample were polished using silicon carbide grit and milli-Q water to eliminate any contamination potentially introduced from cutting using a diamond-tipped blade. The samples were rinsed with ethanol prior to drying in an oven at 60 °C for ~12 h (overnight). The dried sample was then broken into chips and crushed to a fine powder (~30 μm) with no metal contact using a zirconia ceramic dish and puck.

The rhenium-osmium (Re—Os) isotope analysis was carried out at the Durham Geochemistry Centre (Laboratory for Sulfide and Source Rock Geochronology and Geochemistry, and Arthur Holmes Laboratory) at Durham University. The analytical protocol utilises the Cr^{VI}–H_2SO_4 digestion methodology to preferentially liberate hydrogenous Re and Os, and to limit incorporation of any detrital Re and Os (Selby and Creaser, 2003). Approximately 1 g of sample powder with a known amount of mixed ^{190}Os and ^{185}Re tracer (spike) solution and 8 ml of 0.25 g/g Cr^{VI}–H_2SO_4 solution were placed and sealed in to a carius tube and heated at 220 °C for 48 h. Osmium was purified by solvent extraction ($CHCl_3$) and micro-distillation methods (Cohen and Waters, 1996; Birck et al., 1997). Rhenium was separated and purified from the Os-extracted Cr^{VI}–H_2SO_4 solution using NaOH–C_3H_6O solvent extraction

and anion chromatography. The purified Re and Os fractions were loaded onto Ni and Pt filaments, respectively (Selby et al., 2007). Isotopic measurements were determined using a ThermoScientific TRITON mass spectrometer using static Faraday collection for Re and secondary electron multiplier in peak-hopping mode for Os. Total procedural blanks during this study were 15.6 ± 0.45 pg and 0.035 ± 0.007 pg (1σ S.D., $n = 3$) for Re and Os, respectively, with an average $^{187}Os/^{188}Os$ value of 0.18 ± 0.01. Blank contributes less than 1% of the Re and Os budget, except for 7 samples, of which 6 are of Early Triassic age that have blank corrections of up to ~20%.

The initial $^{187}Os/^{188}Os$ composition (Os_i) were calculated using the ^{187}Re decay constant 1.666×10^{-11} yr^{-1} (Smoliar et al., 1996). Due to the relatively large uncertainties of the LA-ICP-MS ages of the volcanic ashes (Liao et al., 2016a, 2016b), each sample's age was estimated using the geochronology of the Wuchiapingian–Changhsingian (254.14 Ma; Shen et al., 2019c) and Permian–Triassic boundaries (251.9 Ma; Shen et al., 2019c), assuming a constant deposition rate throughout the section. The age difference between a sample's real age and the assigned age has negligible effect on the calculated Os isotope initial (Os_i). For example, a 0.5 Myr age difference results in <0.02 variation in the calculated Os_i with the exception for a few samples in the lower part of the section that have higher Re/Os ratios. For these samples the difference in the calculated Os_i can be up to 0.05. Repeat analyses of reference material SDO-1 suggest ≤0.04 variation in calculated Os_i (Du Vivier et al., 2014; Du Vivier et al., 2015).

4. Results

The Re and Os concentrations for the Niushan section range from ~0.1 to 1192 ppb and 6.2 to 4975 ppt (^{192}Os = ~ 2.3–738 ppt), respectively (Table S1; Fig. 2). Stratigraphically, except for the lowest sample in the Longtan Formation, samples within the Dalong Formation (~7–22 m) are enriched in Re and Os (5.1–1191.6 ppb and 155–4975 ppt, respectively), with samples in the Yinkeng Formation (above ~20 m) exhibiting a decline in Re and Os abundance to less than 1 ppb and 21 ppt, respectively. The trend in Re and Os abundance, in general follows the trend with total organic carbon (TOC) (Table S1; Fig. 2).

In the late Wuchiapingian (upper Longtan and basal Dalong Formations), the two analysed samples (LT-17, NS-13) yield radiogenic Os_i values (~1.0 and 1.9, respectively) (Fig. 2). The Os_i value is less radiogenic across the middle Changhsingian (middle Dalong Formation, 14-16 m) (average of samples NS-01, 03, 34, 46, 0.68 ± 0.23, $n = 4$). Between the latter and samples at and above 20 m there is a single sample (NS-80) with a Os_i of 1.72. Approximately 2 m below to the EPME the Os_i are ~0.52 to 0.71 (average 0.62 ± 0.06). Immediately above the negative carbon-isotope anomaly at the EPME interval two samples with distinctly different Re (16.9 and 0.7 ppb) and Os (265.5 and 21.0 ppt) have very similar Os_i values (0.30 and 0.34). The Os_i then rises to 1.14 across the Permian–Triassic boundary, and then returns to 0.53 in the early Triassic.

5. Discussion

5.1. Data evaluation

The Re—Os system has been shown to be disturbed by post-depositional processes (such as weathering and hydrothermal activity), and some of the samples close to the P–T interval have Re and Os values close to the upper continental crust (0.198 ppb Re and 31 ppt Os; Peucker-Ehrenbrink and Jahn, 2001). However, we suggest that the Os isotope values in the Niushan section represent seawater Os isotope values during the Late Permian and Early Triassic based on the following points: 1) the samples were recovered from an active quarry and therefore collected samples were from a freshly exposed surface; 2) utilized samples showed no visible evidence of veining or weathering; 3) analytical protocol employs a CrO_3-H_2SO_4 digestion medium that has been shown to preferentially liberate the hydrogenous Re and Os (Selby and Creaser, 2003; Kendall et al., 2004; Rooney et al., 2011; Xu et al., 2012; Sperling et al., 2014), and 4) the Re—Os systematics of stratigraphically adjacent samples (NS-109, NS-111) possessing significantly different Re and Os budgets yield very similar Os_i values. In addition, the calculated Os_i are geologically plausible and similar to previously reported Os_i values from the Late Permian and Early Triassic sections (Yang et al., 2004; Georgiev et al., 2011, 2015; Schoepfer et al., 2013; Zhao et al., 2015; Liu et al., 2020b).

5.2. Paleogeographic control of Os_i values

The Niushan section records a near-shore delta plain depositional setting during the Wuchiapingian and transition to a marine setting across the Wuchiapingian–Changhsingian boundary interval (Liao et al., 2016a). Both samples in the late Wuchiapingian yield highly radiogenic Os_i values (~1 and 1.9). These values are comparable to those reported from the Lianyuan section in South China (~1.2), which also records a fluvial-deltaic paleogeographic setting expressed by similar siltstone interbedded with thin coalbeds during this time interval (Liu et al., 2019b). These radiogenic Os_i mainly reflect the proximal continental setting of the sites, with the bulk of its Os being derived from continental runoff, with limited contribution of Os from open-marine seawater. The Os_i increase from 1 to 1.9 may reflect increased restriction in response to a fall in sea level and/or tectonic uplift. In contrast to the radiogenic Os isotope signature of the near-shore Lianyuan and Niushan (South China) sections, Wuchiapingian–Changhsingian sections that were deposited in more marine setting (i.e. the Meishan and Shangsi sections in South China, the Buchanan Lake in Canada, Greenland and Norway sections) generally have a less radiogenic Os isotope composition (~ 0.55–0.60; Georgiev et al., 2011; Liu et al., 2019b). Within the marine incursion in the Niushan section, the Os_i values drop to ~0.6 in the upper Changhsingian, and these values are equivalent to that of late Permian seawater Os isotope values which are reconstructed from the continental shelf marine sections of Opal Creek (Canada), Hovea-3 (Australia), and Meishan (China) (Schoepfer et al., 2013; Georgiev et al., 2015, 2020; Zhao et al., 2015; Liu et al., 2020b). Another Os_i increase to ~1.7 is detected in the upper Changhsingian, which likely reflect another pulse of sea level shallowing, as evidenced by the lithology change from shale to carbonates.

5.3. Osmium isotope evidence for volcanism and weathering

Available Os isotope data from the Meishan (South China) and Opal Creek (Canada) sections exhibit multiple unradiogenic Os isotope excursions that are interpreted to reflect episodes of volcanic activities before, during and after the EPME (Schoepfer et al., 2013; Georgiev et al., 2015; Liu et al., 2020b). In contrast, the more deep-water PTB Niushan (water depth of >200 m) section is more distal to that of the shallow-water sections (0–50 m; Meishan/Opal Creek) (Fig. 1) and therefore should reflect a more open marine signature (e.g., Rooney et al., 2016; Jones et al., 2020). Thus, the Os isotope profile from the deep-water PTB Niushan section, coupled with published data from shallow-water PTB sections, provides a more comprehensive understanding of the global marine Os isotope record across the EPME event (Schoepfer et al., 2013; Zhao et al., 2015; Georgiev et al., 2015; Liu et al., 2020b).

An unradiogenic shift in the Os_i composition from ~0.6 to 0.3 is found immediately above the mass extinction interval (EPME, Fig. 2). In theory, the unradiogenic Os isotope shift could be driven by increased input of unradiogenic Os from weathering of magmatic rocks and/or a meteorite impact (Peucker-Ehrenbrink and Ravizza, 2000). However, there is a lack of any convincing evidence for a meteorite impact (Shen et al., 2019b). Considering the volcanic ash layers found in the Niushan section and the studies that have demonstrated the intensive volcanic activity through the Late Permian and Early Triassic (e.g. Payne and

Kump, 2007; Saunders and Reichow, 2009; Burgess et al., 2014; Burgess and Bowring, 2015; Burgess et al., 2017; Liu et al., 2017; Wang et al., 2018; Shen et al., 2019a; Shen et al., 2019b), magmatic activity is a more reasonable interpretation for the unradiogenic Os isotope excursion, possibly linked with intensive volcanism in South China (e.g. Korte and Kozur, 2010; Yin and Song, 2013; Liu et al., 2020b). The Os isotope data here provide further insights into the pattern of the volcanism, and the temporal relationship between volcanism and the mass extinction event. In the Niushan section, an unradiogenic osmium isotope shift is only detected after the EPME, which is in contrast to the Meishan section that exhibits abrupt and intense unradiogenic shifts in Os_i both pre- and post-the mass extinction event (Liu et al., 2020b). We cannot rule out the possibility that the lack of unradiogenic Os_i shift before the mass extinction interval at the Niushan section could have been missed in our sampling approach, however, the interval around the PTB was sampled at a high resolution of ~10 cm, which is comparable to that of the Meishan section. High precision Zircon U—Pb geochronology (CA-ID-TIMS) suggests the Siberian Traps shift from extrusive eruption before the mass extinction to intrusive magmatism during the mass extinction interval, and then back to extrusive eruption (Burgess et al., 2017). The unradiogenic Os isotope excursions thus might correlate with the extrusive phases of the Siberian Traps and the subsequent weathering of the mafic extrusive units.

Unfortunately, sample material for the exact sample that exhibits the largest negative carbon isotope value (NS-107) of the Niushan section is no longer available. However, samples immediately below sample NS-107 show no unradiogenic shift in Os_i, whereas the carbon isotope values have already started to decline (Fig. 2). Nevertheless, the unradiogenic shift in Os_i post the mass extinction interval is detected in both the Niushan and Meishan sections (Fig. 3). A previous study has attributed the difference in the Os isotope profiles between different sections to different magnitude in the volcanic events that are responsible for the Os isotope excursion(s) (Liu et al., 2019b). Those pulses of volcanism that preceded the mass extinction event may be smaller in scale than that post the mass extinction event, and thus the later pulse of volcanism is more widely recorded in the Os isotope oceanic record than that of the earlier volcanic events. It is also possible that the volcanic activity occurred in a more terrestrial location and thus not recorded in the deep-water column, and/or the unradiogenic Os isotope shift identified post EPME in the Niushan section reflects the weathering of the basalt that happened several tens of thousands of years after the volcanism. The latter is also supported by Hg records from both the Meishan and Opal Creek sections that exhibit Hg/TOC anomalies that are generally shown in the intervals below or within the EPME interval, which resulted from synchronous Hg emission during volcanism (Fig. 3; Grasby et al., 2017; Wang et al., 2018; Shen et al., 2019a). The fact that the Niushan section shows a smaller unradiogenic Os_i shift than those recorded in sections representative of a slope depositional environment (Meishan and Opal Creek) suggests that more open ocean deep-water settings were less affected by volcanic activities, and corroborates the deep-water migration of foraminifers around the PTB (Liu et al., 2020c). The latter is driven by toxic compounds released from the Siberian Traps and other volcanic activities in the shallow waters around the Tethys Ocean (Liu et al., 2020c).

Above the unradiogenic shift, the Os_i values show an increase to more radiogenic values, peaking at 1.14, in the Niushan section (Fig. 2). In theory, the increase in Os_i can be caused by either reduced unradiogenic Os flux or increased radiogenic Os input from continental weathering to the water column. Given the active volcanism at this time, invoking an enhanced weathering scenario may be more appropriate to interpret the Os_i trend observed at Niushan. A trend to more radiogenic Os_i following volcanism has also been reported for the shallow-water Meishan section (Fig. 3). In the Meishan section, the Os_i shift to ~1.25 from ~0.6, which is slightly larger than the Os isotope value of 1.14 from the Niushan section (Liu et al., 2020b). A previous study has suggested that in the near-shore regions, the marine residence time of Os, that is, the amount of Os in seawater reservoir divided by the sum of input or output fluxes, will be considerably shorter than the accepted value of *c.* 10^4 yr (e.g. Paquay and Ravizza, 2012; Rooney et al., 2016). The more radiogenic Os_i at Meishan thus may reflect its more proximal setting relative to Niushan, and as a result the increased radiogenic Os flux might be slightly lower than previously estimated (Liu et al., 2020b). At steady state, the seawater osmium isotope composition is determined by the mixing of radiogenic Os input (1.4) and unradiogenic Os input (0.12) given by:

$$R_{sw} = (M_u{*}R_u + M_r{*}R_r) \quad (1)$$

where R_{sw}, R_u and R_r denote the Os isotope compositions of seawater,

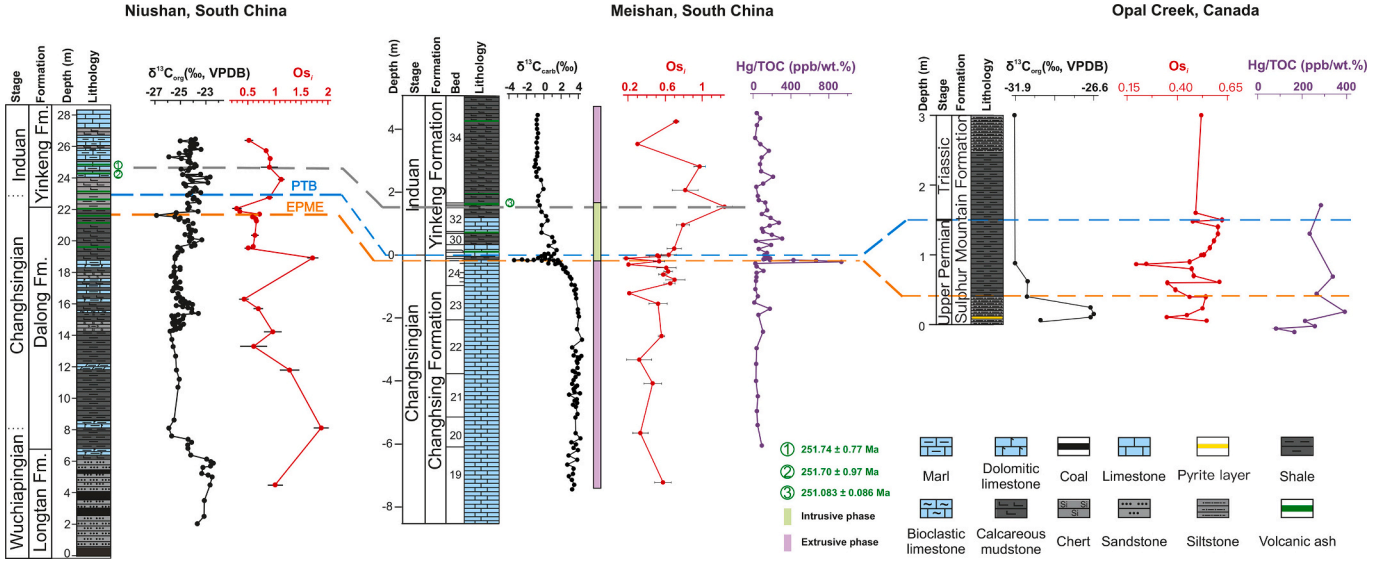

Fig. 3. Correlation of Os_i from the Niushan section, the Meishan section and the Opal Creek (Canada) section. The Niushan $\delta^{13}C_{org}$ data are from Liao et al. (2016a). The Opal Creek section Os_i data are from Schoepfer et al. (2013) and Georgiev et al. (2015); $\delta^{13}C_{org}$ data from Georgiev et al. (2015); Hg/TOC data from Shen et al. (2019a); and the uppermost $\delta^{13}C_{org}$ and Os_i data points represent the average value of all five Triassic samples. The Meishan section $\delta^{13}C_{carb}$ data from Shen et al. (2011), Os_i data from Liu et al. (2020b), Hg/TOC data from Wang et al. (2018) and Grasby et al. (2017). Age in the Meishan section is from CA-TIMS U—Pb zircon dated volcanic ash bed (Burgess et al., 2014). Ages in the Niushan section are LA-ICP-MS U—Pb zircon dated volcanic ash beds (Liao et al., 2016a, 2016b).

unradiogenic input and radiogenic input; M_u and M_r represent the mass of unradiogenic Os input and radiogenic Os input respectively. Assuming a constant weathering input of radiogenic Os, the volcanic Os flux is estimated to have increased ~8 times, based on the Os isotope data from the Meishan section (from 0.6 to 0.2; Liu et al., 2020b). However, using the data of this study (0.6 to 0.3), the volcanic Os input increase is only ~2.7 times. Similarly, for the estimation of radiogenic Os input from weathering, with the assumption of a stable unradiogenic Os input, Os isotope data from the Meishan section suggest a ~ 9 times increase (Liu et al., 2020b). In contrast, Os data from the Niushan section yield an increase of radiogenic Os flux by ~5 times (compared with ~9 times by using a Os_i value of 1.2 from the Meishan section).

The Os_i values then fall from 1.14 to 0.5 above the PTB (Fig. 2). This unradiogenic Os_i shift likely reflects decreasing weathering intensity, as excessive greenhouse volatiles were mitigated by silicate weathering. This is earlier than that inferred from the Sr isotope data, which indicates enhanced weathering until the late Early Triassic (Song et al., 2015). However, Os has a considerably shorter oceanic residence time than Sr (10 kyr vs. 2 Ma). Thus, the Os isotope data would be expected to show a decrease in the Os_i prior to Sr in response to the decreased weathering above the PTB.

5.4. Implications for using $^{187}Os/^{188}Os$ for paleoclimate research

The $^{187}Os/^{188}Os$ composition of sedimentary units has been widely applied to infer the Os-isotope composition of the water column at the time of deposition, and moreover to infer the paleogeography/paleoceanography (e.g. Cohen, 2004; Turgeon and Creaser, 2008; Tejada et al., 2009; Georgiev et al., 2011; Peucker-Ehrenbrink and Ravizza, 2012; Dickson et al., 2015; Liu et al., 2020a). Typically, the more proximal shallow-water sections generally have more radiogenic Os isotope values compared to that of deep-water sections, due to elevated terrestrial Os input with radiogenic Os isotope compositions and/or limited seawater exchange (e.g., Porter et al., 2014; Rooney et al., 2016; Jones et al., 2020). Further, the Os isotope record from near-shore and shelf/slope sections tend to exhibit larger signal excursions relative to those recovered from deep-water sections (e.g., Jones et al., 2020). A similar scenario is also shown with the Paleocene–Eocene thermal maximum initial Os isotope records. For example, the Millville section, which is a near-shore expanded section, has a larger unradiogenic Os isotope composition shift (~0.08) compared with most shelf sections that show unradiogenic Os isotope composition shift of ~0.05 (Dickson et al., 2015; Liu et al., 2019a). Whereas, the pelagic section at Blake Nose (ODP Hole 1051 B) only shows a nominal Os isotope composition shift (~0.01), which is within analytical uncertainty of the Os isotope measurement (Liu et al., 2019a). Another example is the Jurassic Toarcian Oceanic Anoxic Event (T-OAE) that describes a radiogenic osmium isotope shift in response to enhanced weathering. In the near-shore section of Yorkshire (UK), Os isotope increase by ~0.7 (Cohen et al., 2004). Whereas for the more open marine sections of Mochras (UK), East Tributary (North America), and Sakuraguchi-dani (Japan) excursions only increase by ~0.3–0.4 (Percival et al., 2016; Them et al., 2017; Kemp et al., 2020).

In addition to tracking volcanism and/or extraterrestrial impact events, as well as weathering signals, osmium isotopes have also been used to quantify the scale of the event, and even the size of the impactor (if the type of the impactor is known) (Dickson et al., 2015; Liu et al., 2019a; Paquay et al., 2008). Consequently, using Os isotope data from shallow-water sections may yield an overestimation of the degree of the magmatism and/or weathering of radiogenic Os, as well as the size of the impactor. As such, the Os isotope data from deep-water sections might be a more reliable source of data for any numerical models. Thus, wherever possible, such evaluations should be made with data from multiple sections to get a more comprehensive understanding. A similar conclusion can also be drawn by using the T-OAE Os isotope excursion data from near-shore section of Yorkshire (UK) (~0.7 Os_i change) and open marine sections of Mochras (UK), Dotternhausen/Dormettingen (Germany), East Tributary (North America), and Sakuraguchi-dani (Japan) (~0.3–0.4 Os_i change) to estimate the weathering intensity change over the T-OAE (Cohen et al., 2004; Them et al., 2017; van Acken et al., 2019; Kemp et al., 2020).

Also noteworthy, massive volcanism associated with the EPME is also considered to be associated with an increase in greenhouse gas emissions, which resulted in an increase in silicate weathering and organic carbon burial (the negative feedback mechanism; Walker et al., 1981; Jenkyns, 2010). As a result, the unradiogenic Os isotope shift signal driven by volcanism might be dampened by the radiogenic Os input from increased weathering to some extent.

6. Conclusions

The Os isotope stratigraphy across the Permian–Triassic boundary interval of the Niushan section suggests that volcanism and enhanced weathering are associated with the late Permian mass extinction event. Unlike the Os isotope records from Meishan and Opal Creek, the Os isotope data from the Niushan section show no unradiogenic Os isotope excursion immediately before the mass extinction interval. The Niushan section does however exhibit an unradiogenic Os isotope shift following the mass extinction interval. There is also a radiogenic Os isotope shift signal detected above the unradiogenic Os isotope shift, which is interpreted to be caused by enhanced weathering. Both the volcanism and weathering signals are smaller relative to those reported from the Meishan and Opal Creek sections. As such, different paleogeographic settings may record different magnitudes in the Os isotope excursions, and thus any numerical evaluation using Os isotope stratigraphy to model geological events should be treated carefully unless based on multiple sites and/or more open ocean records where possible.

Declaration of Competing Interest

None.

Acknowledgements

We would like to thank Prof. Jian Cao (Nanjing University) for providing the samples for this study. For laboratory support we gratefully acknowledge Antonia Hofmann, Chris Ottley, Geoff Nowell and Emma Ownsworth. We also acknowledge the TOTAL Endowment Fund and the CUG Wuhan Dida Scholarship to DS, China Postdoctoral Science Foundation (20M682934) and the University of Durham and China Scholarship Council to ZL. Finally, we would like to thank David van Acken and one anonymous reviewer for their constructive reviews that greatly improved the manuscript. Data available from an open-source online data repository hosted at Mendeley Data (doi:10.17632/c3864dc938.1).

Appendix A. Supplementary data

Supplementary data to this article can be found online at https://doi.org/10.1016/j.gloplacha.2021.103473.

References

Birck, J.L., Barman, M.R., Capmas, F., 1997. Re-Os isotopic measurements at the femtomole level in natural samples. Geostand. Newslett. 21 (1), 19–27. https://doi.org/10.1111/j.1751-908X.1997.tb00528.x.

Burgess, S.D., Bowring, S.A., 2015. High-precision geochronology confirms voluminous magmatism before, during, and after Earth's most severe extinction. Sci. Adv. 1 (7) https://doi.org/10.1126/sciadv.1500470.

Burgess, S.D., Bowring, S., Shen, S.-z., 2014. High-precision timeline for Earth's most severe extinction. Proc. Natl. Acad. Sci. 111 (9), 3316–3321. https://doi.org/10.1073/pnas.1317692111.

Burgess, S.D., Muirhead, J.D., Bowring, S.A., 2017. Initial pulse of Siberian Traps sills as the trigger of the end-Permian mass extinction. Nat. Commun. 8 (1), 164. https://doi.org/10.1038/s41467-017-00083-9.

Cao, C., Love, G.D., Hays, L.E., Wang, W., Shen, S., Summons, R.E., 2009. Biogeochemical evidence for euxinic oceans and ecological disturbance presaging the end-Permian mass extinction event. Earth Planet. Sci. Lett. 281 (3), 188–201. https://doi.org/10.1016/j.epsl.2009.02.012.

Chen, J., et al., 2016. High-resolution SIMS oxygen isotope analysis on conodont apatite from South China and implications for the end-Permian mass extinction. Palaeogeogr. Palaeoclimatol. Palaeoecol. 448, 26–38. https://doi.org/10.1016/j.palaeo.2015.11.025.

Chu, D., et al., 2020. Ecological disturbance in tropical peatlands prior to marine Permian-Triassic mass extinction. Geology 48 (3), 288–292. https://doi.org/10.1130/g46631.1.

Clarkson, M.O., Kasemann, S.A., Wood, R.A., Lenton, T.M., Daines, S.J., Richoz, S., Ohnemueller, F., Meixner, A., Poulton, S.W., Tipper, E.T., 2015. Ocean acidification and the Permo-Triassic mass extinction. Science 348 (6231), 229–232. https://doi.org/10.1126/science.aaa0193.

Cohen, A.S., 2004. The rhenium–osmium isotope system: applications to geochronological and palaeoenvironmental problems. J. Geol. Soc. 161 (4), 729–734. https://doi.org/10.1144/0016-764903-084.

Cohen, A.S., Waters, F.G., 1996. Separation of osmium from geological materials by solvent extraction for analysis by thermal ionisation mass spectrometry. Anal.Chim. Acta 332 (2–3), 269–275. https://doi.org/10.1016/0003-2670(96)00226-7.

Cohen, A.S., Coe, A.L., Harding, S.M., Schwark, L., 2004. Osmium isotope evidence for the regulation of atmospheric CO_2 by continental weathering. Geology 32 (2), 157–160. https://doi.org/10.1130/G20158.1.

Dal Corso, J., Mills, B.J.W., Chu, D., Newton, R.J., Mather, T.A., Shu, W., Wu, Y., Tong, J., Wignall, P.B., 2020. Permo–Triassic boundary carbon and mercury cycling linked to terrestrial ecosystem collapse. Nat. Commun. 11 (1), 2962. https://doi.org/10.1038/s41467-020-16725-4.

Dickson, A. J., A. S. Cohen, A. L. Coe, M. Davies, E. A. Shcherbinina, and Y. O. Gavrilov (2015), Evidence for weathering and volcanism during the PETM from Arctic Ocean and Peri-Tethys osmium isotope records, Palaeogeogr. Palaeoclimatol. Palaeoecol., 438, 300–307, doi:doi:10.1016/j.palaeo.2015.08.019.

Du Vivier, A.D.C., Selby, D., Sageman, B.B., Jarvis, I., Gröcke, D.R., Voigt, S., 2014. Marine $^{187}Os/^{188}Os$ isotope stratigraphy reveals the interaction of volcanism and ocean circulation during Oceanic Anoxic Event 2. Earth Planet. Sci. Lett. 389, 23–33. https://doi.org/10.1016/j.epsl.2013.12.024.

Du Vivier, A.D.C., Selby, D., Condon, D.J., Takashima, R., Nishi, H., 2015. Pacific $^{187}Os/^{188}Os$ isotope chemistry and U–Pb geochronology: synchroneity of global Os isotope change across OAE 2. Earth Planet. Sci. Lett. 428, 204–216. https://doi.org/10.1016/j.epsl.2015.07.020.

Erwin, D.H., 2006. Extinction: How Life on Earth Nearly Ended 250 Million Years Ago. Princeton University Press.

Garbelli, C., Angiolini, L., Shen, S.-z., 2017. Biomineralization and global change: a new perspective for understanding the end-Permian extinction. Geology 45 (1), 19–22. https://doi.org/10.1130/g38430.1.

Georgiev, S., Stein, H.J., Hannah, J.L., Bingen, B., Weiss, H.M., Piasecki, S., 2011. Hot acidic Late Permian seas stifle life in record time. Earth Planet. Sci. Lett. 310 (3), 389–400. https://doi.org/10.1016/j.epsl.2011.08.010.

Georgiev, S.V., Stein, H.J., Hannah, J.L., Henderson, C.M., Algeo, T.J., 2015. Enhanced recycling of organic matter and Os-isotopic evidence for multiple magmatic or meteoritic inputs to the Late Permian Panthalassic Ocean, Opal Creek, Canada. Geochim. Cosmochim. Acta 150, 192–210. https://doi.org/10.1016/j.gca.2014.11.019.

Georgiev, S.V., Stein, H.J., Yang, G., Hannah, J.L., Böttcher, M.E., Grice, K., Holman, A.I., Turgeon, S., Simonsen, S., Cloquet, C., 2020. Late Permian–Early Triassic environmental changes recorded by multi-isotope (Re-Os-N-Hg) data and trace metal distribution from the Hovea-3 section, Western Australia. Gondwana Res. 88, 353–372. https://doi.org/10.1016/j.gr.2020.07.007.

Grasby, S.E., Shen, W., Yin, R., Gleason, J.D., Blum, J.D., Lepak, R.F., Hurley, J.P., Beauchamp, B., 2017. Isotopic signatures of mercury contamination in latest Permian oceans. Geology 45 (1), 55–58. https://doi.org/10.1130/g38487.1.

Grice, K., Cao, C., Love, G.D., Böttcher, M.E., Twitchett, R.J., Grosjean, E., Summons, R. E., Turgeon, S.C., Dunning, W., Jin, Y., 2005. Photic zone euxinia during the Permian-Triassic superanoxic event. Science 307 (5710), 706–709. https://doi.org/10.1126/science.1104323.

Henderson, C.M., 1989. Absaroka Sequence—The lower Absaroka Sequence: Upper Carboniferous and Permian (chapter 10). In: Ricketts, B. (Ed.), Basin Analysis— The Western Canada Sedimentary Basin: Canadian Society of Petroleum Geologists Special Publication, pp. 203–217.

Hinojosa, J.L., Brown, S.T., Chen, J., DePaolo, D.J., Paytan, A., Shen, S.-z., Payne, J.L., 2012. Evidence for end-Permian Ocean acidification from calcium isotopes in biogenic apatite. Geology 40 (8), 743–746. https://doi.org/10.1130/g33048.1.

Hu, G., Liao, Z., Wang, L., Cao, J., Tan, X., 2019. Transient fluctuation in paleoclimate at the end of Permian: New constraints from paleosol carbonates in the Erlongkou section, Chongqing, southwestern China. J. Asian Earth Sci. 173, 225–236. https://doi.org/10.1016/j.jseaes.2019.01.027.

Jenkyns, H.C., 2010. Geochemistry of oceanic anoxic events. Geochem. Geophys. Geosyst. 11 (3) https://doi.org/10.1029/2009gc002788.

Jin, Y., Wang, Y., Henderson, C., Wardlaw, B.R., Shen, S., Cao, C., 2006. The Global Boundary Stratotype Section and Point (GSSP) for the base of Changhsingian Stage (Upper Permian). Episodes 29 (3), 175–182.

Joachimski, M.M., Lai, X., Shen, S., Jiang, H., Luo, G., Chen, B., Chen, J., Sun, Y., 2012. Climate warming in the latest Permian and the Permian–Triassic mass extinction. Geology 40 (3), 195–198. https://doi.org/10.1130/g32707.1.

Jones, M.M., Sageman, B.B., Selby, D., Jicha, B.R., Singer, B.S., Titus, A.L., 2020. Regional chronostratigraphic synthesis of the Cenomanian-Turonian Oceanic Anoxic Event 2 (OAE2) interval, Western Interior Basin (USA): new Re-Os chemostratigraphy and $^{40}Ar/^{39}Ar$ geochronology. GSA Bull. https://doi.org/10.1130/b35594.1.

Kemp, D.B., Selby, D., Izumi, K., 2020. Direct coupling between carbon release and weathering during the Toarcian oceanic anoxic event. Geology. https://doi.org/10.1130/g47509.1.

Kendall, B.S., Creaser, R.A., Ross, G.M., Selby, D., 2004. Constraints on the timing of Marinoan "Snowball Earth" glaciation by $^{187}Re–^{187}Os$ dating of a Neoproterozoic, post-glacial black shale in Western Canada. Earth Planet. Sci. Lett. 222 (3), 729–740. https://doi.org/10.1016/j.epsl.2004.04.004.

Korte, C., Kozur, H.W., 2010. Carbon-isotope stratigraphy across the Permian–Triassic boundary: a review. J. Asian Earth Sci. 39 (4), 215–235. https://doi.org/10.1016/j.jseaes.2010.01.005.

Liao, Z., W. Hu, J. Cao, X. Wang, S. Yao, and Y. Wan (2016a), Permian–Triassic boundary (PTB) in the Lower Yangtze Region, southeastern China: a new discovery of deep-water archive based on organic carbon isotopic and U–Pb geochronological studies, Palaeogeogr. Palaeoclimatol. Palaeoecol., 451, 124–139, doi:doi:10.1016/j.palaeo.2016.03.004.

Liao, Z., Hu, W., Cao, J., Wang, X., Yao, S., Wu, H., Wan, Y., 2016b. Heterogeneous volcanism across the Permian–Triassic Boundary in South China and implications for the Latest Permian Mass Extinction: new evidence from volcanic ash layers in the Lower Yangtze Region. J. Asian Earth Sci. 127, 197–210. https://doi.org/10.1016/j.jseaes.2016.06.003.

Liu, S.-A., Wu, H., Shen, S.-z., Jiang, G., Zhang, S., Lv, Y., Zhang, H., Li, S., 2017. Zinc isotope evidence for intensive magmatism immediately before the end-Permian mass extinction. Geology 45 (4), 343–346. https://doi.org/10.1130/g38644.1.

Liu, X., Song, H., Bond, D.P.G., Tong, J., Benton, M.J., 2020c. Migration controls extinction and survival patterns of foraminifers during the Permian-Triassic crisis in South China. Earth Sci. Rev. 209, 103329. https://doi.org/10.1016/j.earscirev.2020.103329.

Liu, Z., Horton, D.E., Tabor, C., Sageman, B.B., Percival, L.M.E., Gill, B.C., Selby, D., 2019a. Assessing the Contributions of comet impact and volcanism toward the climate perturbations of the Paleocene-Eocene thermal Maximum. Geophys. Res. Lett. 46 (24), 14798–14806. https://doi.org/10.1029/2019gl084818.

Liu, Z., Selby, D., Zhang, H., Zheng, Q., Shen, S., Sageman, B.B., Grasby, S.E., Beauchamp, B., 2019b. Osmium-isotope evidence for volcanism across the Wuchiapingian–Changhsingian boundary interval. Chem. Geol. 529, 119313. https://doi.org/10.1016/j.chemgeo.2019.119313.

Liu, Z., Selby, D., Hackley, P.C., Over, D.J., 2020a. Evidence of wildfires and elevated atmospheric oxygen at the Frasnian−Famennian boundary in New York (USA): implications for the Late Devonian mass extinction. GSA Bull. https://doi.org/10.1130/b35457.1.

Liu, Z., Selby, D., Zhang, H., Shen, S., 2020b. Evidence for volcanism and weathering during the Permian-Triassic mass extinction from Meishan (South China) osmium isotope record. Palaeogeogr. Palaeoclimatol. Palaeoecol. 553, 109790. https://doi.org/10.1016/j.palaeo.2020.109790.

Paquay, F.S., Ravizza, G., 2012. Heterogeneous seawater $^{187}Os/^{188}Os$ during the Late Pleistocene glaciations. Earth Planet. Sci. Lett. 349–350, 126–138. https://doi.org/10.1016/j.epsl.2012.06.051.

Paquay, F.S., Ravizza, G.E., Dalai, T.K., Peucker-Ehrenbrink, B., 2008. Determining chondritic impactor size from the marine osmium isotope record. Science 320 (5873), 214–218. https://doi.org/10.1126/science.1152860.

Payne, J.L., Kump, L.R., 2007. Evidence for recurrent Early Triassic massive volcanism from quantitative interpretation of carbon isotope fluctuations. Earth Planet. Sci. Lett. 256 (1), 264–277. https://doi.org/10.1016/j.epsl.2007.01.034.

Percival, L.M.E., Cohen, A.S., Davies, M.K., Dickson, A.J., Hesselbo, S.P., Jenkyns, H.C., Leng, M.J., Mather, T.A., Storm, M.S., Xu, W., 2016. Osmium isotope evidence for two pulses of increased continental weathering linked to Early Jurassic volcanism and climate change. Geology 44 (9), 759–762. https://doi.org/10.1130/G37997.1.

Peucker-Ehrenbrink, B., Jahn, B.-m., 2001. Rhenium-osmium isotope systematics and platinum group element concentrations: loess and the upper continental crust. Geochem. Geophys. Geosyst. 2 (10) https://doi.org/10.1029/2001GC000172 n/a-n/a.

Peucker-Ehrenbrink, B., Ravizza, G., 2000. The marine osmium isotope record. Terra Nova 12 (5), 205–219. https://doi.org/10.1046/j.1365-3121.2000.00295.x.

Peucker-Ehrenbrink, B., Ravizza, G., 2012. Osmium Isotope Stratigraphy. In: Gradstein, F.M., Ogg, J.G., Schmitz, M.D., Ogg, G.M. (Eds.), The Geologic Time Scale. Elsevier, Boston, pp. 145–166. https://doi.org/10.1016/b978-0-444-59425-9.00008-1.

Porter, S.J., Smith, P.L., Caruthers, A.H., Hou, P., Gröcke, D.R., Selby, D., 2014. New high resolution geochemistry of Lower Jurassic marine sections in western North America: a global positive carbon isotope excursion in the Sinemurian? Earth Planet. Sci. Lett. 397, 19–31. https://doi.org/10.1016/j.epsl.2014.04.023.

Rooney, A.D., Chew, D.M., Selby, D., 2011. Re–Os geochronology of the Neoproterozoic–Cambrian Dalradian Supergroup of Scotland and Ireland: implications for Neoproterozoic stratigraphy, glaciations and Re–Os systematics. Precambrian Res. 185 (3–4), 202–214. https://doi.org/10.1016/j.precamres.2011.01.009.

Rooney, A.D., Selby, D., Lloyd, J.M., Roberts, D.H., Lückge, A., Sageman, B.B., Prouty, N. G., 2016. Tracking millennial-scale Holocene glacial advance and retreat using

osmium isotopes: insights from the Greenland ice sheet. Quat. Sci. Rev. 138, 49–61. https://doi.org/10.1016/j.quascirev.2016.02.021.
Saunders, A., Reichow, M., 2009. The Siberian Traps and the End-Permian mass extinction: a critical review. Chin. Sci. Bull. 54 (1), 20–37. https://doi.org/10.1007/s11434-008-0543-7.
Schoepfer, S.D., Henderson, C.M., Garrison, G.H., Foriel, J., Ward, P.D., Selby, D., Hower, J.C., Algeo, T.J., Shen, Y., 2013. Termination of a continent-margin upwelling system at the Permian–Triassic boundary (Opal Creek, Alberta, Canada). Glob. Planet. Change 105, 21–35. https://doi.org/10.1016/j.gloplacha.2012.07.005.
Selby, D., Creaser, R.A., 2003. Re–Os geochronology of organic rich sediments: an evaluation of organic matter analysis methods. Chem. Geol. 200 (3–4), 225–240. https://doi.org/10.1016/S0009-2541(03)00199-2.
Selby, D., Creaser, R.A., Fowler, M.G., 2007. Re–Os elemental and isotopic systematics in crude oils. Geochim. Cosmochim. Acta 71 (2), 378–386. https://doi.org/10.1016/j.gca.2006.09.005.
Shen, J., Algeo, T.J., Hu, Q., Xu, G., Zhou, L., Feng, Q., 2013. Volcanism in South China during the Late Permian and its relationship to marine ecosystem and environmental changes. Glob. Planet.Change 105, 121–134. https://doi.org/10.1016/j.gloplacha.2012.02.011.
Shen, J., Chen, J., Algeo, T.J., Yuan, S., Feng, Q., Yu, J., Zhou, L., O'Connell, B., Planavsky, N.J., 2019a. Evidence for a prolonged Permian–Triassic extinction interval from global marine mercury records. Nat. Commun. 10 (1), 1563. https://doi.org/10.1038/s41467-019-09620-0.
Shen, S., et al., 2019b. A sudden end-Permian mass extinction in South China. GSA Bull. https://doi.org/10.1130/B31909.1.
Shen, S., et al., 2019c. Permian integrative stratigraphy and timescale of China. Sci. China Earth Sci. 62 (1), 154–188. https://doi.org/10.1007/s11430-017-9228-4.
Shen, S.-Z., et al., 2011. Calibrating the end-permian mass extinction. Science 334 (6061), 1367–1372. https://doi.org/10.1126/science.1213454.
Smoliar, M.I., Walker, R.J., Morgan, J.W., 1996. Re-Os ages of group IIA, IIIA, IVA, and IVB iron meteorites. Science 271 (5252), 1099. https://doi.org/10.1126/science.271.5252.1099.
Song, H., et al., 2015. Integrated Sr isotope variations and global environmental changes through the Late Permian to early Late Triassic. Earth Planet.Sci. Lett. 424, 140–147. https://doi.org/10.1016/j.epsl.2015.05.035.
Song, H., et al., 2021. Conodont calcium isotopic evidence for multiple shelf acidification events during the Early Triassic. Chem. Geol. 562, 120038. https://doi.org/10.1016/j.chemgeo.2020.120038.
Sperling, E.A., Rooney, A.D., Hays, L., Sergeev, V.N., Vorob'eva, N.G., Sergeeva, N.D., Selby, D., Johnston, D.T., Knoll, A.H., 2014. Redox heterogeneity of subsurface waters in the Mesoproterozoic ocean. Geobiology 12 (5), 373–386. https://doi.org/10.1111/gbi.12091.
Sun, Y., Joachimski, M.M., Wignall, P.B., Yan, C., Chen, Y., Jiang, H., Wang, L., Lai, X., 2012. Lethally hot temperatures during the early Triassic greenhouse. Science 338 (6105), 366–370. https://doi.org/10.1126/science.1224126.
Tejada, M.L.G., Kuroda, J., Suzuki, K., Ohkouchi, N., Sakamoto, T., Tatsumi, Y., Coccioni, R., Mahoney, J.J., 2009. Ontong Java Plateau eruption as a trigger for the early Aptian oceanic anoxic event. Geology 37 (9), 855–858. https://doi.org/10.1130/G25763A.1.
Them, T.R., Gill, B.C., Selby, D., Gröcke, D.R., Friedman, R.M., Owens, J.D., 2017. Evidence for rapid weathering response to climatic warming during the Toarcian Oceanic Anoxic Event. Sci. Rep. 7 (1), 5003. https://doi.org/10.1038/s41598-017-05307-y.
Turgeon, S.C., Creaser, R.A., 2008. Cretaceous oceanic anoxic event 2 triggered by a massive magmatic episode. Nature 454 (7202), 323–326. https://doi.org/10.1038/nature07076.
van Acken, D., Tütken, T., Daly, J.S., Schmid-Röhl, A., Orr, P.J., 2019. Rhenium-osmium geochronology of the Toarcian Posidonia Shale, SW Germany. Palaeogeogr. Palaeoclimatol. Palaeoecol. 534, 109294. https://doi.org/10.1016/j.palaeo.2019.109294.
Walker, J.C.G., Hays, P.B., Kasting, J.F., 1981. A negative feedback mechanism for the long-term stabilization of Earth's surface temperature. J. Geophys. Res. 86 (C10), 9776–9782. https://doi.org/10.1029/JC086iC10p09776.
Wang, X., Cawood, P.A., Zhao, H., Zhao, L., Grasby, S.E., Chen, Z.-Q., Wignall, P.B., Lv, Z., Han, C., 2018. Mercury anomalies across the end Permian mass extinction in South China from shallow and deep water depositional environments. Earth Planet. Sci. Lett. 496, 159–167. https://doi.org/10.1016/j.epsl.2018.05.044.
Wang, Y., Jin, Y., 2000. Permian palaeogeographic evolution of the Jiangnan Basin, South China. Palaeogeogr. Palaeoclimatol. Palaeoecol. 160 (1), 35–44. https://doi.org/10.1016/S0031-0182(00)00043-2.
Wignall, P.B., Twitchett, R.J., 1996. Oceanic Anoxia and the End Permian Mass Extinction. Science 272 (5265), 1155–1158. https://doi.org/10.1126/science.272.5265.1155.
Xu, G., Hannah, J.L., Bingen, B., Georgiev, S., Stein, H.J., 2012. Digestion methods for trace element measurements in shales: paleoredox proxies examined. Chem. Geol. 324–325, 132–147. https://doi.org/10.1016/j.chemgeo.2012.01.029.
Yang, G., Chen, J., Du, A., Qu, W., Yu, G., 2004. Re-Os dating of Mo-bearing black shale of the Laoyaling deposit. Tongling, Anhui Province, China 49, 1396–1400. https://doi.org/10.1360/03wd0325.
Yin, H., Song, H., 2013. Mass extinction and Pangea integration during the Paleozoic-Mesozoic transition. Sci. China Earth Sci. 56 (11), 1791–1803. https://doi.org/10.1007/s11430-013-4624-3.
Yin, H.F., Zhang, K.X., Tong, J.N., Yang, Z.Y., W, S.B., 2001. The Global Stratotype Section and Point (GSSP) of the Permian-Triassic Boundary. Episodes 24, 102–114.
Zhao, H., Li, C., Jiang, X.J., Zhou, L.M., Li, X.W., Qu, W.J., Du, A.D., 2015. Enrichment Mechanism of Re-Os in Limestone from Changxing Permian-Triassic Boundary in Zhejiang. Acta Geol. Sin. 89, 1783–1791 (in Chinese).
Ziegler, A.M., Hulver, M.L., Rowley, D.B., 1997. Permian world topography and climate. In: Martini, I.P. (Ed.), Late Glacial and Postglacial Environmental Changes–Quaternary, Carboniferous–Permian and Proterozoic. Oxford University Press, New York, pp. 111–146.